Am J Transl Res 2026;18(1):717-728
www.ajtr.org /ISSN:1943-8141/AJTR0167142

Original Article

Predicting invasiveness of subsolid nodules: a HRCT-based model for lung adenocarcinoma

Feng Li[1*], Changhui Xue[2*], Yang Chen[1], Dabao Shi[1], Fei Ye[1], Honglei Huang[3]

[1]Department of Medical Imaging, Nanping First Hospital Affiliated to Fujian Medical University, Nanping 353000, Fujian, China; [2]Department of Orthopedics, Nanping First Hospital Affiliated to Fujian Medical University, Nanping 353000, Fujian, China; [3]Department of Radiology, Nanping First Hospital Affiliated to Fujian Medical University, Nanping 353000, Fujian, China. [*]Equal contributors and co-first authors.

Received July 1, 2025; Accepted December 27, 2025; Epub January 15, 2026; Published January 30, 2026

Abstract: Background: Subsolid nodules (SSNs) pose a diagnostic challenge in lung adenocarcinoma management. High-resolution computed tomography (HRCT) allows detailed characterization of SSNs, aiding in distinguishing pathological subtypes. Objective: To investigate the correlation between HRCT features and pathological subtypes of SSNs, and their association with nodule size and morphological features. Methods: Clinical and HRCT data from 84 patients with surgically confirmed lung adenocarcinoma were retrospectively analyzed. All patients underwent preoperative CT scans, with lesions measuring ≤3.0 cm and a ground-glass opacity component ≥50%. The evaluated CT characteristics included leison size, lobulation, spiculation, pleural indentation, and CT values. Pathological diagnosis were established according to the latest classification standards. Results: Significant differences were observed among AIS, MIA, and IAC groups in age, lobulation, spiculation, and nodule size (all P<0.01). IAC showed larger size (90.9% between 8-10 mm) and more aggressive features than AIS (57.6% ≤8 mm). Advanced vascular and bronchial patterns were associated with invasive subtypes (P<0.001). EGFR+ tumors exhibited larger size and higher CT values. Multivariate analysis identified age ≥55, lesion diameter ≥8.51 mm, and bronchial pattern as significant predictors for distinguishing MIA from IAC. Conclusion: HRCT features effectively reflect pathological invasiveness of SSNs and can assist in differentiating lung adenocarcinoma subtypes, providing valuable information for diagnosis and treatment planning.

Keywords: Subsolid nodules, HRCT (high-resolution computed tomography), lung adenocarcinoma, Chinese lung adenocarcinoma patients, microvessel density EGFR mutation

Introduction

Lung cancer remains the leading cause of cancer-related mortality globally, with lung adenocarcinoma (LAC) being the most prevalent histological subtype of non-small cell lung cancer (NSCLC) [1]. The prognosis of LAC is highly dependent on its stage at diagnosis, underscoring the critical importance of early and accurate detection. The widespread adoption of low-dose computed tomography (LDCT) screening has led to a significant increase in the detection of subsolid nodules (SSNs), which include pure ground-glass nodules (GGNs) and part-solid nodules (PSNs) [2, 3].

These detected SSNs often represent a spectrum of preinvasive to invasive adenocarcinomas, such as atypical adenomatous hyperplasia (AAH), adenocarcinoma in situ (AIS), minimally invasive adenocarcinoma (MIA), and invasive adenocarcinoma (IAC). Given that each carry vastly different management implications and prognostic outcomes, these SSNs pose a unique diagnostic challenge for clinicians [4]. High-resolution computed tomography (HRCT) serves as a fundamental tool for the non-invasive characterization of subsolid nodules (SSNs) by revealing critical morphological features such as lobulation, spiculation, and pleural indentation, as well as quantifying variations in density. HRCT advancements have refined diagnostic precision, facilitating enhanced discrimination of SSNs' pathological nature (benign vs. malignant), growth tracking, and malignancy risk prediction with greater preci-

https://doi.org/10.62347/WMVL6705

sion [5]. However, the exact relationship between these imaging characteristics and the underlying pathological subtypes is not yet fully understood, particularly in specific populations. Current management guidelines rely heavily on nodule size and solid component growth for decision-making [6]. A more nuanced and predictive model integrating a wider array of quantitative and qualitative HRCT characteristics could significantly refine pre-operative diagnosis, potentially avoiding unnecessary interventions for indolent lesions or advocating for timely resection of aggressive ones.

The integration of radiological phenotypes with genomic biomarkers, such as epidermal growth factor receptor (EGFR) mutation status, is a cornerstone of precision medicine in advanced NSCLC but is less explored in early-stage SSNs [7]. Understanding whether specific HRCT features can serve as non-invasive surrogates for aggressive biology or mutation status could provide a powerful tool for risk stratification. Clarifying the link between imaging traits and pathological stages can aid in formulating clinical management guidelines and follow-up protocols for LAC patients presenting with SSNs, thereby enabling risk-stratified, individualized interventions and ultimately improving clinical outcomes [8].

The primary objective of this study is to rigorously evaluate the correlations between a comprehensive set of HRCT imaging characteristics, including both morphological signs and CT attenuation values, and the definitive pathological subtypes (AIS, MIA, and IAC). A key innovation of our work is the additional exploration of the association between these radiological features and EGFR mutation status. We hypothesize that specific HRCT features can reliably predict not only pathological invasiveness but also underlying genomic profiles. Our findings may provide clinicians with a more robust imaging-based framework for differentiating between indolent and aggressive SSNs. This work will inform more personalized management strategies, guide decision-making regarding surgical timing versus follow-up, and contribute to the development of integrated diagnostic models that combine imaging and genomics to enhance precision medicine in early-stage lung adenocarcinoma.

Methods

Study design and patient selection

This single-center, retrospective study was approved by the Nanping First Hospital Affiliated to Fujian Medical University Review Board with a waiver for informed consent. We initially screened patients with pathologically confirmed LAC who underwent surgical resection between January 2020 and December 2022 at Nanping First Hospital, affiliated with Fujian Medical University. All patients underwent preoperative contrast-enhanced dual-energy spectral computed tomography (DESCT) two weeks prior to surgery.

Inclusion criteria: (1) Availability of complete clinicopathological and imaging records for retrospective analysis; (2) Adult patients (≥18 years) with a confirmed histopathological diagnosis of LAC from the surgical specimen; (3) Availability of complete molecular testing results, including EGFR mutation status and Ki-67 labeling index; (4) Availability of preoperative DESCT images with dual-energy spectral imaging (GSI) acquisition that met the diagnostic quality requirements.

Exclusion criteria: (1) History of any other malignant tumors or previous neoadjuvant therapy (chemotherapy, radiotherapy, or immunotherapy) prior to the CT scan; (2) Postoperative pathology confirming benign lesions, metastatic tumors to the lung, or non-adenocarcinoma malignancies; (3) Incomplete clinical, pathological, or genetic data that precluded comprehensive analysis; (4) Inadequate DESCT image quality due to severe artifacts (e.g., from respiratory motion, metal implants) or insufficient contrast enhancement, which could affect accurate quantitative analysis.

After applying these criteria, 150 patients were ultimately enrolled in the final cohort. The detailed patient selection process is illustrated in **Figure 1**.

Data extraction and management

Data extraction was performed independently by two trained radiologists who were blinded to the pathological results and genetic status. A standardized data collection form was used to

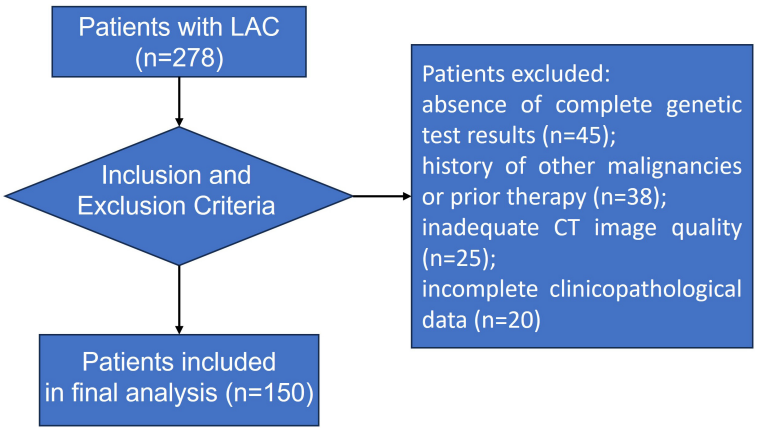

Figure 1. Flow chart for patient selection in this study.

extract the following data from the electronic medical records and the Picture Archiving and Communication System (PACS):

• Demographics: age and sex.

• Imaging features: DESCT images were acquired using the scanner following a standardized protocol. Scanning parameters included: tube voltage of 80 kVp and 140 kVp with a tin filter, tube current of 210 mAs, and collimation of 128 × 0.6 mm. Images were reconstructed with a slice thickness of 1 mm. Features extracted included nodule size, morphological characteristics (e.g., lobulation, spiculation, pleural indentation), and quantitative parameters (e.g., iodine concentration, spectral Hounsfield unit curve slope) [9].

• Pathological results: Hematoxylin and eosin-stained sections were reviewed by two experienced pathologists (blinded to the imaging findings) to confirm the diagnosis. The pathological diagnosis and classification of LAC, specifically the categories of AIS, MIA, and IAC, were performed according to the 2021 WHO classification of lung tumors [10]. In cases of discrepant diagnosis between the two pathologists, a joint review session was held under a multi-head microscope to re-examine the slides and reach a final consensus.

• Molecular biomarkers: EGFR mutation status (detected by PCR-based assays) and Ki-67 labeling index (determined by immunohistochemistry [IHC]) were recorded from pathology reports [11, 12]. For EGFR mutation analysis, genomic DNA was extracted from formalin-fixed, paraffin-embedded (FFPE) tumor tissues. The presence of common EGFR mutations (including exon 19 deletions and exon 21 L858R mutation) was detected by the amplification refractory mutation system (ARMS), using the EGFR 29 Mutations Detection Kit (ADx-EG0X, AmoyDx, Xiamen, China) following the manufacturer's protocol. Ki-67 expression was evaluated by IHC on tumor tissue sections using an automated immunostainer (BenchMark XT, Roche Ventana, Tucson, AZ, USA) and a monoclonal rabbit anti-human Ki-67 antibody (ab16667, Abcam, USA). The labeling index was quantified by counting the percentage of positively stained tumor cell nuclei. Assessment was performed in areas of highest nuclear staining (hotspots), and at least 1,000 tumor cells were counted per case at high-power magnification (×400). The Ki-67 labeling index was treated as a continuous variable and also as a binary variable for analysis. A high Ki-67 expression was defined as a labeling index ≥20%, based on established criteria and the quantification method described above. Representative photomicrographs of Ki-67 staining across different pathological subtypes (AIS, MIA, IAC) are provided in Figure S1.

The extracted data were managed in a dedicated database. Any discrepancies in the extracted data were resolved by consensus between the two readers or by consulting a senior radiologist.

Outcome measures

The primary outcome of this study was the pathological invasiveness grade of lung adenocarcinoma. The secondary outcomes included EGFR mutation status, which was dichotomized as positive (mutant) or negative (wild-type) based on the ARMS-PCR analysis (as detailed in Molecular biomarkers section).

Statistical analysis

Continuous variables were expressed as mean ± standard deviation or median (interquartile range), based on their distribution, and categor-

ical variables were presented as frequencies (percentages). The normality of continuous data was assessed using the Shapiro-Wilk test.

For comparisons across the three pathological subtypes (AIS, MIA, and IAC): An omnibus test was first conducted to determine if any significant differences existed among the groups; for continuous variables, the Kruskal-Wallis H test (for non-normally distributed data) or one-way ANOVA (for normally distributed data) was used for this overall comparison; for categorical variables, the Fisher's exact test was used; If the omnibus test result was significant (P<0.05), post-hoc pairwise comparisons were performed. For continuous variables, Dunn's test with a Bonferroni adjustment was used for non-parametric data, while Tukey's HSD test was employed for parametric data. For categorical variables, pairwise Fisher's exact tests with Bonferroni-adjusted significance levels were conducted.

Inter-observer agreement for the assessment of imaging features was evaluated using the intraclass correlation coefficient (ICC) for continuous variables or Cohen's kappa statistic for categorical variables.

The primary statistical analyses involved binary logistic regression models to identify independent predictors of invasiveness. Given the ordinal nature of pathological progression (AIS→MIA→IAC), the dependent variable was defined in two clinically relevant ways: Model 1 (IAC vs. Non-IAC): Comparing Invasive Adenocarcinoma (IAC) against the combined group of pre-invasive and minimally invasive lesions (AIS + MIA). Model 2 (Invasive vs. Pre-Invasive): Comparing all lesions containing invasive components (MIA + IAC) against pre-invasive lesions (AIS).

Variables with a *p*-value <0.1 in univariate analysis were included in the multivariate model. The final multivariate model was constructed using a backward stepwise elimination method based on the likelihood ratio test, with a significance level of P<0.05 for variable retention. Model fit was assessed using the Hosmer-Lemeshow test. Results were presented as odds ratios (OR) with 95% confidence intervals (CI). The discriminatory performance of the significant multivariate logistic regression model (Model 1: IAC vs. Non-IAC) was evaluated using receiver operating characteristic (ROC) curve analysis, and the area under the curve (AUC) was calculated. The DeLong test was used to compare AUCs if necessary.

All statistical analyses were performed using SPSS software (version 26.0; IBM Corp., Armonk, NY, USA) and R software (version 4.0.2; R Foundation for Statistical Computing, Vienna, Austria) with the dunn.test and pROC packages. A two-sided *p*-value <0.05 was considered statistically significant, except for post-hoc pairwise comparisons, where the Bonferroni-adjusted significance level was applied.

Results

Patient and nodule characteristics

A total of 84 patients with subsolid nodules (SSNs) were included in the final analysis. The baseline clinical and radiological characteristics of the cohort are summarized in **Table 1**. The mean age of the participants was 55.4 ± 12.5 years, with a female predominance (65.5%). The nodules had a mean diameter of 8.51 ± 1.47 mm and an average CT attenuation of -283.79 ± 217.59 HU. The majority of nodules were part-solid (60.2%) and located in the right upper lobe (31.0%).

Differentiation of pathological subtypes (AIS, MIA, and IAC)

Significant differences in clinical and radiological features were observed across the three pathological subtypes (AIS, MIA, and IAC), as detailed in **Table 2**.

• Clinical Features: Patients with IAC were significantly older (63.7 ± 9.2 years) than those with MIA (56.0 ± 10.2 years) or AIS (49.4 ± 13.2 years) (P=0.0001). No significant difference in sex distribution was found.

• Morphological Features: Malignancy-associated morphological signs became increasingly prevalent with higher invasiveness. Spiculation was absent in AIS but was observed in 58.6% of MIA and 90.9% of IAC nodules (P<0.0001). Lobulation was also significantly more pronounced in IAC (50.0% with severe

Table 1. Clinical and radiological characteristics of included patients

Variables	Patients (n=84)
Age	55.4 ± 12.5
Sex	84 (100)
Male	29 (34.5)
Female	55 (65.5)
Location	84 (100)
LLL	19 (22.6)
LUL	16 (19.1)
RLL	17 (20.2)
RML	6 (7.1)
RUL	26 (31.0)
Morphologic features	
Clear margin	44 (52.4)
Lobulated sign	84
none	12 (14.3)
slight	32 (38.1)
modertate	23 (27.4)
severe	17 (20.2)
Spiculated sign	37 (44.1)
Vacuole sign	15 (17.9)
Pleural indentation	84
none	1 (1.2)
one	38 (45.2)
more than two	45 (53.6)
Morphology	84
circular	35 (41.7)
oval	20 (23.8)
irregular	29 (34.5)
Mean diameter (mm)	8.51 ± 1.47 8.51 (7.04-9.98)
Mean CT value (HU)	-283.79 ± 217.59 -283.79 (-501 to -66)
Artery	-256.08 ± 207.08 -256.08 (-463 to -49)
Vein	-253.28 ± 203.36 -253.28 (457 to -49)
Vascular category	84 (100)
I. No relation	5 (6.0)
II. Vessels normal	24 (28.6)
III. Vessels twisted and dilated	32 (38.1)
IV. More complex	23 (27.4)
Bronchial category	84 (100)
I. Course truncated	8 (9.5)
II. Solid distortion and dilation	26 (31.0)
III. Ground-glass distortion and dilati	19 (22.6)
IV. Course normal	11 (13.1)
V. Bypassing	20 (23.8)

lobulation) compared to AIS and MIA (P<0.0001). IAC nodules were predominantly irregular in shape (63.6%), whereas AIS nodules were primarily circular (P<0.0001).

• Quantitative Features: Both mean nodule diameter and CT attenuation values increased significantly with invasiveness. IAC nodules had the largest diameter (9.50 ± 0.70 mm) and highest density (-88.01 ± 173.17 HU), while AIS nodules had the smallest size (7.74 ± 1.56 mm) and lowest density (-397.45 ± 155.91 HU) (P<0.001).

• Vascular and Bronchial Relations: More complex vascular patterns (twisted/dilated) and bronchial alterations (truncation/distortion) were strongly associated with the IAC subtype (P<0.0001 for both).

The representative HRCT images illustrating the spectrum of features from AIS to IAC are shown in **Figure 2**. The distribution of pathological subtypes across different nodule sizes is further visualized in **Figure 3**, confirming that larger nodules (8-10 mm) were significantly more likely to be IAC (90.9%), whereas smaller nodules (≤8 mm) were predominantly AIS (57.6%) (P=0.001).

Associations with EGFR mutation status

As shown in **Table 3**, EGFR mutation status (positive vs. negative) was not associated with any specific morphological features or SSN subtype. However, EGFR-positive tumors exhibited significantly larger diameters and higher CT attenuation values (higher HU) com-

Subtype of SSNs	84 (100)
NSN	33 (39.3)
PSN	51 (60.7)

Note: AIS, adenocarcinoma in situ; MIA, minimally invasive adenocarcinoma; IAC, invasive adenocarcinoma; RLL, right lower lobe; RML, right middle lobe; RUL, right upper lobe; LLL, left lower lobe; LUL, left upper lobe; CT, computed tomography; HU, Hounsfield units; SSN, subsolid nodules; NSN, nonsolid nodule; PSN, part-solid nodule.

pared to EGFR-negative tumors. Furthermore, as presented in **Table 4**, no significant correlation was found between EGFR status and the pathological subtypes (AIS, MIA, IAC).

Predictive modeling for invasiveness

Univariate logistic regression analysis (**Table 5**) demonstrated that age ≥55 years, diameter ≥8.51 mm, and bronchial category (types I/II) were significant predictors for differentiating minimally invasive adenocarcinoma from invasive adenocarcinoma, whereas other radiological features did not show statistical significance in this analysis. A multivariate logistic regression model was developed to differentiate MIA from IAC (**Table 6**). Age ≥55 years, lesion diameter ≥8.51 mm, and the presence of specific bronchial patterns were identified as independent significant predictors. A predictive model incorporating these variables demonstrated excellent discriminatory power, with an AUC of 0.873 (95% CI: 0.779-0.967, P<0.001) in the ROC analysis (**Figure 4**). In contrast, no significant predictors were identified to differentiate AIS from MIA in the multivariate analysis (Tables S1-S3).

Discussion

Our comprehensive examination of HRCT features in Chinese patients with SSNs confirms and extends the established role of imaging in predicting the pathological stage of LAC. The present findings demonstrate that quantitative and qualitative HRCT characteristics are closely associated with tumor invasiveness, providing a non-invasive insight into underlying tumor biology.

The strong correlation between increasing nodule size and invasiveness (IAC: 9.50 ± 0.70 mm vs. AIS: 7.74 ± 1.56 mm) aligns with the fundamental principle of tumor growth [13]. Larger size often reflects a greater burden of proliferative cells and the accumulated potential for invasion through the basement membrane, which may explain why nodules exceeding 8 mm frequently necessitate more aggressive management [14]. Beyond lesion size alone, the morphological progression from smooth, well-defined AIS nodules to spiculated and lobulated IAC lesions is particularly indicative of increasing invasiveness. The near-ubiquitous presence of spiculation in IAC (90.9%) and its absence in AIS suggests that this feature is a radiological hallmark of a pro-invasive tumor microenvironment. Recent studies utilizing AI-enhanced HRCT have further validated spiculation as a key independent predictor of invasiveness, underscoring its reliability [15-17]. These spiculations likely represent a desmoplastic stromal reaction and fibrotic band formation elicited by the invasive tumor cells, as previously described [18]. Similarly, the observed increase in vascular complexity (twisted/dilated vessels) and bronchial alterations with advancing stage underscores the tumor's ability to recruit and remodel its local vasculature to support its growth, a phenomenon well-documented in oncology [8].

A pivotal finding of our study is the significant difference in CT attenuation values across pathological subtypes. The progression from low-attenuation AIS (-397.45 ± 155.91 HU) to higher-attenuation IAC (-88.01 ± 173.17 HU) likely mirrors the underlying histopathological changes. AIS, representing lepidic growth without invasion, is characterized by tumor cells lining intact alveolar structures, preserving airspace and resulting in lower density. In contrast, IAC exhibits invasive patterns such as acinar, papillary, or solid growth, which replace the air-filled parenchyma with cellular tissue, fibrosis, and possible collapse, thereby increasing radiological density [19]. This transition from air to tissue dominance provides a mechanistic explanation for the increasing CT values and enhances our understanding of how imaging phenotypes reflect histological progression. Emerging multi-omics research, including proteogenomic studies, suggests that this radiological transition may reflect profound biological shifts during invasion, such as dysregulated cholesterol metabolism and increased endoplasmic reticulum stress, thereby establishing

Table 2. Comparison of clinical and radiological characteristics across three patient groups

Variables	AIS	IAC	MIA	F/U/χ^2	*P* value
Number	33	22	29		
Age	49.4 ± 13.2	63.7 ± 9.2	56.0 ± 10.2	10.710	<0.001[a]
Sex				1.313	0.519[c]
Male	9 (27.3)	9 (40.9)	11 (37.9)		
Female	24 (72.7)	13 (59.1)	18 (62.1)		
Location				9.453	0.320[c]
LLL	8 (24.2)	7 (31.8)	4 (13.8)		
LUL	5 (15.2)	3 (13.6)	8 (27.6)		
RLL	4 (12.1)	7 (31.8)	6 (20.7)		
RML	2 (6.1)	1 (4.6)	3 (10.3)		
RUL	14 (42.4)	4 (18.2)	8 (27.6)		
Morphologic features				5.479	0.065
Clear margin	13 (39.4)	11 (50.0)	20 (67.0)		
Lobulated sign				36.210	<0.001[c]
none	11 (33.3)	0	1 (3.5)		
slight	16 (48.5)	3 (13.6)	13 (44.8)		
modertate	5 (15.2)	8 (36.4)	10 (34.5)		
severe	1 (3.0)	11 (50.0)	5 (17.2)		
Spiculated sign	0	20 (90.9)	17 (58.6)	48.080	<0.001[c]
Vacuole sign	4	4 (90.9)	7 (58.6)		0.467[c]
Pleural indentation	33	22	29		0.025[c]
none	0	1 (4.6)	0		
one	20 (60.6)	5 (22.7)	13 (44.8)		
more than two	13 (39.4)	16 (72.7)	16 (55.2)		
Morphology	33	22	28		<0.001[c]
circular	33 (100)	0	2 (7.1)		
oval	0	8 (36.4)	11 (39.3)		
irregular	0	14 (63.6)	16 (55.2)		
Mean diameter (mm)	7.74 ± 1.56 7.74 (6.18-9.30)	9.50 ± 0.70 9.50 (8.80-10.20)	8.63 ± 1.35 8.63 (7.28-9.98)	12.090	<0.001[b]
Mean CT value (HU)	-397.45 ± 155.91 -397.45 (-553 to -242)	-88.01 ± 173.17 -88.01 (-261 to 85)	-306.89 ± 209.32 -397.45 (-516 to -98)	19.750	<0.001
Artery	-358.79 ± 144.50 -358.79 (-503 to -214)	-46.79 ± 122.61 -46.79 (-169 to 76)	-315.09 ± 198.08 -315.09 (-513 to -117)	27.420	<0.001
Vein	-343.91 ± 150.87 -343.91 (-495 to -193)	-44.88 ± 117.46 -44.88 (-162 to 73)	-310.36 ± 194.98 -310.36 (-505 to -115)	25.690	<0.001
Vascular category				77.670	<0.001
I. No relation	5 (15.1)	0	0		
II. Vessels normal	24 (72.7)	0	0		
III. Vessels twisted and dilated	4 (12.1)	8 (36.4)	20 (69.0)		
IV. More complex	0	14 (63.6)	9 (31.0)		
Bronchial category				77.100	<0.001
I. Course truncated	0	7 (31.8)	1 (3.5)		
II. Solid distortion and dilation	0	11 (50.0)	15 (51.7)		
III. Ground-glass distortion and dilati	4 (12.1)	4 (18.2)	11 (37.9)		
IV. Course normal	9 (27.3)	0	2 (6.9)		
V. Bypassing	20 (60.6)	0	0		
Subtype of SSNs				28.270	<0.001
NSN	24 (72.7)	1 (4.54)	8 (27.6)		
PSN	9 (27.3)	21 (95.46)	21 (72.4)		

Notes: a, Anova-test; b, Kruskal-Wallis-test; c, Pearson χ^2 test; AIS, adenocarcinoma in situ; MIA, minimally invasive adenocarcinoma; IAC, invasive adenocarcinoma; RLL, right lower lobe; RML, right middle lobe; RUL, right upper lobe; LLL, left lower lobe; LUL, left upper lobe; CT, computed tomography; HU, Hounsfield units; SSN, subsolid nodules; NSN, nonsolid nodule; PSN, part-solid nodule.

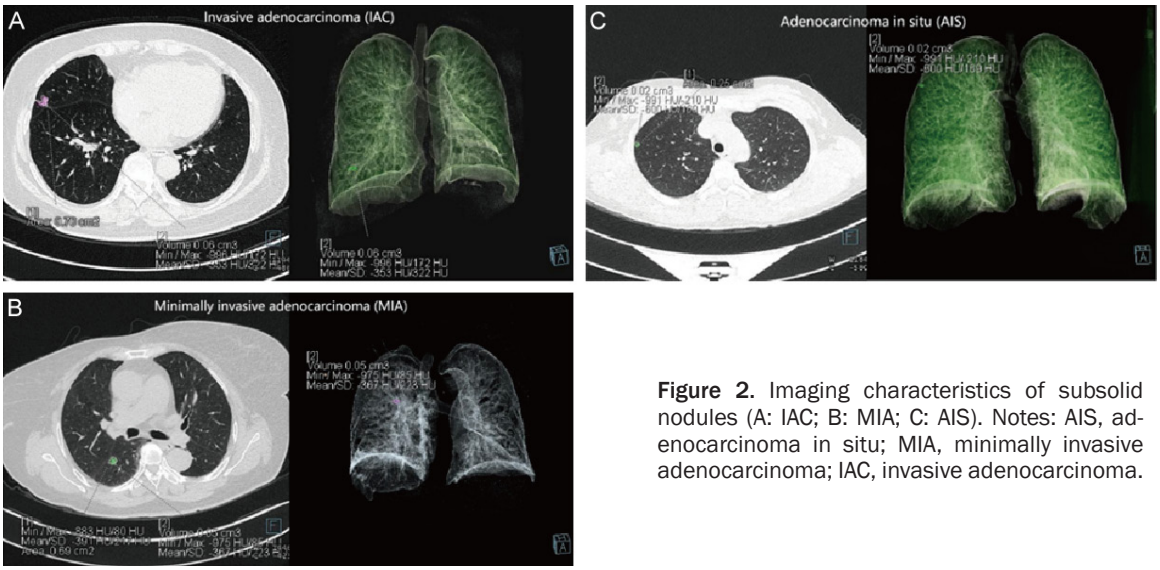

Figure 2. Imaging characteristics of subsolid nodules (A: IAC; B: MIA; C: AIS). Notes: AIS, adenocarcinoma in situ; MIA, minimally invasive adenocarcinoma; IAC, invasive adenocarcinoma.

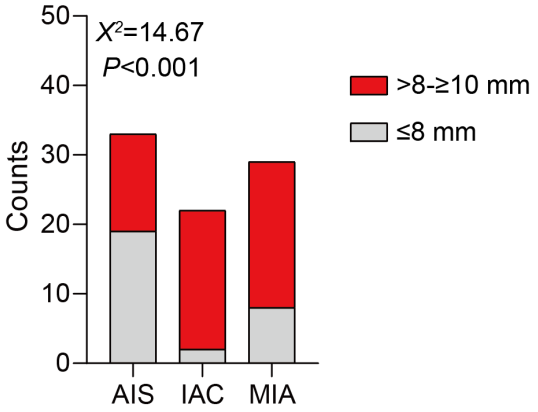

Figure 3. Composition of pathological subtypes across different diameter groups. Stacked bar chart showing the proportional distribution of subsolid nodules in two diameter groups (≤8 mm, >8-≥10 mm) within each pathological subtype: adenocarcinoma in situ (AIS), minimally invasive adenocarcinoma (MIA), and invasive adenocarcinoma (IAC). This figure displays the distribution of pathological subtypes of subsolid nodules (SSNs) across different diameter ranges. The subtypes include: Adenocarcinoma in Situ (AIS) with 33 cases (39.3%), Invasive Adenocarcinoma (IAC) with 26.2%, and Minimally Invasive Adenocarcinoma (MIA) with 34.5%. For AIS, 57.6% had a mean diameter ≤8 mm and 42.4% had a diameter of 8-10 mm. For IACs, the respective percentages were 9.1% and 90.9%; for MIAs, they were 27.6% and 72.4%. A chi-square test showed significant differences among the three subtypes across diameter groups (P=0.001).

a direct link between imaging features and molecular pathogenesis [20, 21].

The novelty of our work lies in the application of DESCT within a Chinese cohort, demonstrating that a model integrating age, lesion diameter, and bronchial changes can effectively discriminate between invasive and non-invasive lesions. This approach provides a pragmatic and quantitative framework using existing clinical CT protocols. Notably, the frontier of technical refinement is rapidly advancing, as exemplified by a recent study that developed a machine learning model based on ultra-high-resolution CT (2048-matrix) radiomic features, which achieved an even higher predictive performance (AUC: 0.863) [22]. This comparison not only validates the critical role of imaging data quality but also points to a promising future direction: the potential integration of spectral information from DESCT with high-resolution morphometric details to build a next-generation, fused predictive model.

Despite these insights, several limitations must be acknowledged. First, the retrospective, single-center design may introduce selection bias and limits the generalizability of our findings. Second, the sample size, particularly for the IAC subgroup, was relatively small, which may affect the stability of the statistical models and necessitate validation in a larger, prospective multicenter cohort. Third, while we correlated imaging features with EGFR status, a more comprehensive genomic analysis incorporating other drivers (e.g., ALK, ROS1, KRAS) could provide a deeper understanding of the molecular determinants of radiological phenotypes. Future studies should focus on longitudinal observations of SSNs to capture radiological evolution and integrate a broader panel of molecular biomarkers to build predictive mod-

Table 3. Diagnostic CT features associated with EGFR mutation status in lung adenocarcinoma [EGFR(-) vs. EGFR(+)]

Variable	EGFR (-)	EGFR (+)	$T/U/\chi^2$	*P* value
Number	39	45		
Morphologic features			1.368	0.850
smooth	24 (61.54)	20 (44.44)		
lobulated	34 (87.18)	38 (84.44)		
spiculated	12 (30.77)	15 (33.33)		
vacuolated	6 (15.38)	9 (20.00)		
pleural indentation	37 (94.87)	43 (95.56)		
Morphology			3.633	0.163
circular	12 (30.77)	23 (51.11)		
oval	10 (25.64)	9 (20.00)		
irregular	17 (43.59)	13 (28.89)		
Mean diameter (mm)	8.11 ± 1.68	8.86 ± 1.19	2.384	0.020
Mean CT value (HU)	-326.95 (-610.6, 99)	-149.9 (-752.6, 61.6)	1.172	0.011
Subtype of SSNs			0.092	0.761
NSN	16 (41.03)	17 (37.78)		
PSN	23 (58.97)	28 (62.22)		

Notes: EGFR, epidermal growth factor receptor; HU, Hounsfield units; SSN, subsolid nodules; NSN, nonsolid nodule; PSN, part-solid nodule.

Table 4. Pathological subtype distribution in EGFR-positive (+) vs. EGFR-negative (-) lung adenocarcinomas

Variable	EGRF (-)	EGRF (+)	χ^2	*P* value
Number	39	45		
AIS	16 (41.03)	17 (37.78)	0.147	0.761
IAC	10 (25.64)	12 (28.89)	0.011	0.915
MIA	13 (33.33)	16 (35.56)	0.046	0.831

Notes: EGFR, epidermal growth factor receptor; AIS, adenocarcinoma in situ; MIA, minimally invasive adenocarcinoma; IAC, invasive adenocarcinoma.

Table 5. Univariate logistic regression analysis of significant factors differentiating MIA from IAC

	Category/Definition	OR (95% CI)	*P*-value
Age	≥55 years vs <55 years	3.8 (1.2-12.1)	0.023
Diameter	≥8.51 mm vs <8.51 mm	4.2 (1.3-13.5)	0.016
Lobulated sign	Moderate/Severe vs None/Slight	1.8 (0.4-8.0)	0.450
Spiculated sign	Present vs Absent	3.1 (0.5-18.9)	0.220
Pleural indentation	>1 vs ≤1	2.1 (0.7-6.3)	0.180
Morphology	Irregular vs Circular/Oval	1.4 (0.5-3.9)	0.520
Mean CT value	≥-200 HU vs <-200 HU	2.5 (0.5-12.5)	0.260
Vascular category	III/IV vs I/II	2.3 (0.8-6.6)	0.120
Bronchial category	I/II vs III/IV/V	8.5 (2.6-27.8)	<0.001
Subtype of SSNs	PSN vs NSN	2.0 (0.3-13.5)	0.470

Notes: HU, Hounsfield units; SSN, subsolid nodules; NSN, nonsolid nodule; PSN, part-solid nodule; MIA, minimally invasive adenocarcinoma; IAC, invasive adenocarcinoma.

Table 6. Multivariate logistic regression analysis of significant factors differentiating MIA from IAC

	B	S.D	Wald	*P* value	OR	95% CI
Age	2.715	1.047	6.722	0.010	15.111	1.94-117.71
Diameter	2.820	1.212	5.411	0.020	16.775	1.56-180.54
Bronchial category	-4.147	1.543	7.221	0.007	0.016	0.001-0.325

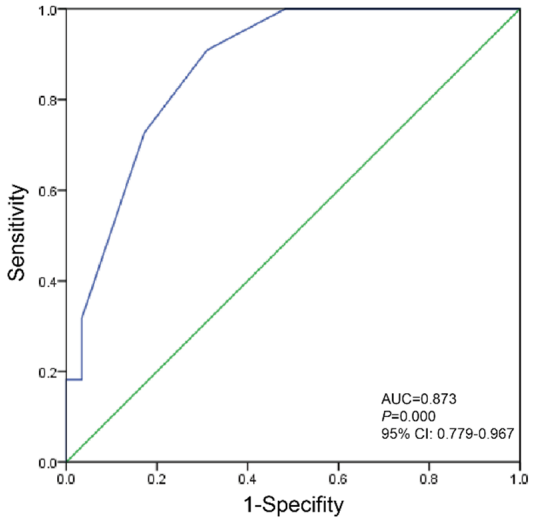

Figure 4. ROC curve analysis of the predictive model for IAC detection using significant MIA/IAC discriminators. Notes: AIS, adenocarcinoma in situ; MIA, minimally invasive adenocarcinoma; IAC, invasive adenocarcinoma.

els that are both radiologically and biologically informed [7]. Furthermore, the integration of cutting-edge imaging technologies like photon-counting CT, which offers ultra-high spatial resolution, could further refine feature analysis and improve non-invasive characterization [23-25].

Conclusion

This study demonstrates significant correlations between DESCT parameters and pathological grades, suggesting that this imaging modality may enhance the reliability of tumor staging. Conclusively, DESCT facilitates tailored therapeutic approaches through more precise tumor characterization, underscoring the necessity of incorporating advanced imaging systems in lung cancer diagnostics.

Acknowledgements

This work was supported by Fujian Provincial Natural Science Foundation of China (Grant number: 2021J011432), Fujian provincial health technology project (Grant number: 2021QNB013), and Fujian Provincial Natural Science Foundation (Grant number: 2025J01-1659).

Disclosure of conflict of interest

None.

Address correspondence to: Honglei Huang, Department of Radiology, Nanping First Hospital Affiliated to Fujian Medical University, Nanping 353000, Fujian, China. Tel: +86-0599-8888120; E-mail: hhlct2020@126.com

References

[1] Siegel RL, Miller KD, Fuchs HE and Jemal A. Cancer statistics, 2022. CA Cancer J Clin 2022; 72: 7-33.

[2] National Lung Screening Trial Research Team; Aberle DR, Adams AM, Berg CD, Black WC, Clapp JD, Fagerstrom RM, Gareen IF, Gatsonis C, Marcus PM and Sicks JD. Reduced lung-cancer mortality with low-dose computed tomographic screening. N Engl J Med 2011; 365: 395-409.

[3] de Koning HJ, van der Aalst CM, de Jong PA, Scholten ET, Nackaerts K, Heuvelmans MA, Lammers JJ, Weenink C, Yousaf-Khan U, Horeweg N, van 't Westeinde S, Prokop M, Mali WP, Mohamed Hoesein FAA, van Ooijen PMA, Aerts JGJV, den Bakker MA, Thunnissen E, Verschakelen J, Vliegenthart R, Walter JE, Ten Haaf K, Groen HJM and Oudkerk M. Reduced lung-cancer mortality with volume CT screening in a randomized trial. N Engl J Med 2020; 382: 503-513.

[4] Naidich DP, Bankier AA, MacMahon H, Schaefer-Prokop CM, Pistolesi M, Goo JM, Macchiarini P, Crapo JD, Herold CJ, Austin JH and Travis WD. Recommendations for the management of subsolid pulmonary nodules detected at CT: a statement from the Fleischner Society. Radiology 2013; 266: 304-317.

[5] Aoki T, Nakata H, Watanabe H, Nakamura K, Kasai T, Hashimoto H, Yasumoto K and Kido M. Evolution of peripheral lung adenocarcinomas: CT findings correlated with histology and tumor

doubling time. AJR Am J Roentgenol 2000; 174: 763-768.
[6] MacMahon H, Naidich DP, Goo JM, Lee KS, Leung ANC, Mayo JR, Mehta AC, Ohno Y, Powell CA, Prokop M, Rubin GD, Schaefer-Prokop CM, Travis WD, Van Schil PE and Bankier AA. Guidelines for management of incidental pulmonary nodules detected on CT images: from the fleischner society 2017. Radiology 2017; 284: 228-243.
[7] Shaw AT, Yeap BY, Mino-Kenudson M, Digumarthy SR, Costa DB, Heist RS, Solomon B, Stubbs H, Admane S, McDermott U, Settleman J, Kobayashi S, Mark EJ, Rodig SJ, Chirieac LR, Kwak EL, Lynch TJ and Iafrate AJ. Clinical features and outcome of patients with non-small-cell lung cancer who harbor EML4-ALK. J Clin Oncol 2009; 27: 4247-4253.
[8] Travis WD, Asamura H, Bankier AA, Beasley MB, Detterbeck F, Flieder DB, Goo JM, MacMahon H, Naidich D, Nicholson AG, Powell CA, Prokop M, Rami-Porta R, Rusch V, van Schil P and Yatabe Y; International Association for the Study of Lung Cancer Staging and Prognostic Factors Committee and Advisory Board Members. The IASLC lung cancer staging project: proposals for coding T categories for subsolid nodules and assessment of tumor size in part-solid tumors in the forthcoming eighth edition of the TNM classification of lung cancer. J Thorac Oncol 2016; 11: 1204-1223.
[9] Lu GM, Zhao Y, Zhang LJ and Schoepf UJ. Dual-energy CT of the lung. AJR Am J Roentgenol 2012; 199 Suppl: S40-53.
[10] Nicholson AG, Tsao MS, Beasley MB, Borczuk AC, Brambilla E, Cooper WA, Dacic S, Jain D, Kerr KM, Lantuejoul S, Noguchi M, Papotti M, Rekhtman N, Scagliotti G, van Schil P, Sholl L, Yatabe Y, Yoshida A and Travis WD. The 2021 WHO classification of lung tumors: impact of advances since 2015. J Thorac Oncol 2022; 17: 362-387.
[11] Wei DM, Chen WJ, Meng RM, Zhao N, Zhang XY, Liao DY and Chen G. Augmented expression of Ki-67 is correlated with clinicopathological characteristics and prognosis for lung cancer patients: an up-dated systematic review and meta-analysis with 108 studies and 14,732 patients. Respir Res 2018; 19: 150.
[12] Li AR, Chitale D, Riely GJ, Pao W, Miller VA, Zakowski MF, Rusch V, Kris MG and Ladanyi M. EGFR mutations in lung adenocarcinomas: clinical testing experience and relationship to EGFR gene copy number and immunohistochemical expression. J Mol Diagn 2008; 10: 242-248.
[13] Hasegawa M, Sone S, Takashima S, Li F, Yang ZG, Maruyama Y and Watanabe T. Growth rate of small lung cancers detected on mass CT screening. Br J Radiol 2000; 73: 1252-1259.
[14] Henschke CI, Yip R, Smith JP, Wolf AS, Flores RM, Liang M, Salvatore MM, Liu Y, Xu DM and Yankelevitz DF; International Early Lung Cancer Action Program Investigators. CT screening for lung cancer: part-solid nodules in baseline and annual repeat rounds. AJR Am J Roentgenol 2016; 207: 1176-1184.
[15] Xiong TW, Gan H, Lv FJ, Zhang XC, Fu BJ and Chu ZG. Artificial intelligence-measured nodule mass for determining the invasiveness of neoplastic ground glass nodules. Quant Imaging Med Surg 2024; 14: 6698-6710.
[16] Wen Y, Wu W, Liufu Y, Pan X, Zhang Y, Qi S and Guan Y. Differentiation of granulomatous nodules with lobulation and spiculation signs from solid lung adenocarcinomas using a CT deep learning model. BMC cancer 2024; 24: 875.
[17] Zou Z, Niu H, Cha Y, Yang J and Han W. Diagnostic value of combined high-resolution computed tomography and artificial intelligence-aided diagnosis system in prediction of benign and malignant pulmonary ground-glass nodules. IJ Radiology 2023; 20: e135104.
[18] Lee HY, Choi YL, Lee KS, Han J, Zo JI, Shim YM and Moon JW. Pure ground-glass opacity neoplastic lung nodules: histopathology, imaging, and management. AJR Am J Roentgenol 2014; 202: W224-233.
[19] Godoy MC and Naidich DP. Subsolid pulmonary nodules and the spectrum of peripheral adenocarcinomas of the lung: recommended interim guidelines for assessment and management. Radiology 2009; 253: 606-622.
[20] Zyla J, Marczyk M, Prazuch W, Sitkiewicz M, Durawa A, Jelitto M, Dziadziuszko K, Jelonek K, Kurczyk A, Szurowska E, Rzyman W, Widłak P and Polanska J. Combining low-dose computer-tomography-based radiomics and serum metabolomics for diagnosis of malignant nodules in participants of lung cancer screening studies. Biomolecules 2023; 14: 44.
[21] Pierri M, Ciani G, Brunese MC, Lauro G, Terracciano S, Iorizzi M, Nardone V, Chini MG, Bifulco G, Cappabianca S and Reginelli A. Advancing non-small-cell lung cancer management through multi-omics integration: insights from genomics, metabolomics, and radiomics. Diagnostics (Basel) 2025; 15: 2586.
[22] Yanagawa M, Nagatani Y, Hata A, Sumikawa H, Moriya H, Iwano S, Tsuchiya N, Iwasawa T, Ohno Y and Tomiyama N. Effect of spatial resolution on the diagnostic performance of machine-learning radiomics model in lung adenocarcinoma: comparisons between normal- and high-spatial-resolution imaging for predicting

invasiveness. Jpn J Radiol 2025; 43: 2003-2017.
[23] Gaillandre Y, Duhamel A, Flohr T, Faivre JB, Khung S, Hutt A, Felloni P, Remy J and Remy-Jardin M. Ultra-high resolution CT imaging of interstitial lung disease: impact of photon-counting CT in 112 patients. Eur Radiol 2023; 33: 5528-5539.
[24] Si-Mohamed SA, Miailhes J, Rodesch PA, Boccalini S, Lacombe H, Leitman V, Cottin V, Boussel L and Douek P. Spectral photon-counting CT technology in chest imaging. J Clin Med 2021; 10: 5757.
[25] Fanni SC, Ambrosini I, Caputo FP, Cuibari ME, Deri D, Guarracino A, Guidi C, Uggenti V, Varanini G, Neri E, Cioni D, Scaglione M and Masala S. A narrative review of photon-counting CT and radiomics in cardiothoracic imaging: a promising match? Diagnostics (Basel) 2025; 15: 2631.

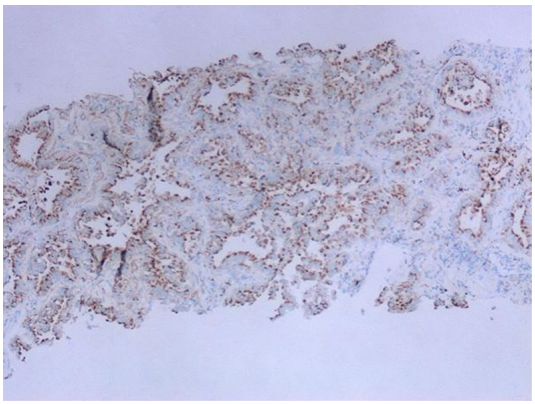

Figure S1. Representative Ki-67 expression dected by immunohistochemistry.

Table S1. Univariate logistic regression analysis for differentiating AIS from MIA

	Category/Definition	OR (95% CI)	*P*-value
Age	≥55 years vs <55 years	1.62 (0.58-4.49)	0.355
Diameter	≥8 mm vs <8 mm	1.95 (0.73-5.21)	0.182
Lobulated sign	Moderate/Severe vs None/Slight	1.78 (0.66-4.78)	0.255
Spiculated sign	Present vs Absent	2.41 (0.45-12.98)	0.305
Mean CT value	≥-300 HU vs <-300 HU	1.88 (0.69-5.13)	0.216
Vascular category	III/IV vs I/II	2.15 (0.74-6.25)	0.160
Bronchial category	I/II/III vs IV/V	1.92 (0.70-5.26)	0.202
Subtype of SSNs	PSN vs NSN	1.55 (0.55-4.35)	0.406

Notes: AIS, adenocarcinoma in situ; MIA, minimally invasive adenocarcinoma; SSN, subsolid nodules; NSN, nonsolid nodule; PSN, part-solid nodule.

Table S2. Multivariate logistic regression analysis for differentiating AIS from IAC

	Category/Definition	OR (95% CI)	*P*-value
Age	≥55 years vs <55 years	2.25 (0.79-6.41)	0.128
Diameter	≥9 mm vs <9 mm	2.88 (0.97-8.55)	0.047
Lobulated sign	Moderate/Severe vs None/Slight	3.12 (0.99-9.80)	0.041
Spiculated sign	Present vs Absent	5.12 (0.88-29.79)	0.069
Mean CT value	≥-150 HU vs <-150 HU	3.45 (0.98-12.20)	0.044
Vascular category	III/IV vs I/II	3.88 (0.94-16.04)	0.061
Bronchial category	I/II vs III/IV/V	4.12 (0.89-19.05)	0.070
Subtype of SSNs	PSN vs NSN	3.76 (0.82-17.24)	0.089

Notes: AIS, adenocarcinoma in situ; IAC, invasive adenocarcinoma; SSN, subsolid nodules; NSN, nonsolid nodule; PSN, part-solid nodule.

Table S3. Multivariate logistic regression analysis for differentiating AIS from IAC

	OR (95% CI)	*P*-value
Diameter (≥9 mm)	2.15 (0.68-6.82)	0.195
Lobulated sign (Moderate/Severe)	2.42 (0.72-8.15)	0.156
Mean CT value (≥-150 HU)	2.78 (0.81-9.55)	0.105

Notes: AIS, adenocarcinoma in situ; IAC, invasive adenocarcinoma.